Photodissociation spectroscopy and dynamics of the methylthio radical (CH_3S)

Ryan T. Bise, Hyeon Choi, Henrik B. Pedersen,[a] David H. Mordaunt,[b] and Daniel M. Neumark
Department of Chemistry, University of California, Berkeley, California 94720 and Chemical Sciences Division, Lawrence Berkeley National Laboratories, Berkeley, California 94720

(Received 1 September 1998; accepted 2 October 1998)

The photodissociation spectroscopy and dynamics of the CH_3S and CD_3S radicals have been investigated using fast radical beam photofragment spectroscopy of the $\tilde{A}\ ^2A_1 \leftarrow \tilde{X}\ ^2E$ electronic band ($T_0 \cong 26\,400\ cm^{-1}$) and an unstructured band near $45\,600\ cm^{-1}$. At all energies, only one major channel, $CH_3(\tilde{X}\ ^2A_2'') + S(^3P_j)$, was observed. Photofragment yield spectra for the $\tilde{A}\ ^2A_1 \leftarrow \tilde{X}\ ^2E$ electronic band show resolved vibrational progressions extending well beyond those seen in laser-induced fluorescence studies of this band. Photofragment translational energy distributions yield the $S(^3P_j)$ fine-structure distribution for each vibrational level of the CH_3 product. Photofragment angular distributions were found to be highly anisotropic ($\beta = -0.2$ to -1.0 ± 0.1) with increasing anisotropy at higher photon energies. The results yield a refined heat of formation for CH_3S (1.346 ± 0.018 eV) as well as the mechanism by which the $\tilde{A}\ ^2A_1$ state is predissociated. Results at $45\,600\ cm^{-1}$ imply that dissociation occurs on the repulsive $\tilde{B}\ ^2A_2$ state. © *1999 American Institute of Physics.* [S0021-9606(99)04201-4]

I. INTRODUCTION

Photodissociation of polyatomic molecules provides a rich probe of excited state potential energy surfaces and their interactions. Measurements of photofragment yield spectra, translational energy distributions, product branching ratios, and fine-structure distributions, probe the detailed coupling of excited electronic states with the dissociation continuum.[1–3] While there have been many photodissociation studies of stable closed-shell molecules over the past 15 years, corresponding studies of open-shell radicals have been limited. Our laboratory has demonstrated the ability to generate a well-characterized source of radicals via photodetachment of negative ions, allowing us to perform photodissociation experiments on reactive open-shell species. In this article, we present the ultraviolet photodissociation spectroscopy and dynamics of the methylthio radical (CH_3S).

The methylthio radical has been proposed as an important intermediate in atmospheric oxidation of naturally occurring sulfur species such as dimethyl sulfide (CH_3SCH_3), dimethyl disulfide (CH_3SSCH_3) and methyl mercaptan (CH_3SH).[4] There have been numerous spectroscopic studies of the methylthio radical since its first spectroscopic observation by Callear and Dickson,[5] a diffuse absorption band centered at $45\,770\ cm^{-1}$. Anion photoelectron and photodetachment spectroscopy,[6–8] microwave[9] and infrared spectroscopy,[10] and electronic emission[11] studies have provided information regarding the geometry, spin–orbit splitting and vibrational frequencies of the $\tilde{X}\ ^2E$ ground state.

The excited $\tilde{A}\ ^2A_1$ state has also been characterized in detail through laser-induced fluorescence (LIF) experiments on the $\tilde{A}\ ^2A_1 \leftarrow \tilde{X}\ ^2E$ transition.[12–16] Vibrationally-resolved measurements show progressions in the totally symmetric C–S stretch (ν_3) and CH_3 umbrella mode (ν_2) modes.[12,13,15–18] The weak 6_0^1 Jahn-Teller active transition involving the methyl rocking mode has also been observed.[15,17] Rotationally resolved LIF experiments by Miller and co-workers[14] show that the C–S bond distance increases by 0.3 Å and the HCS bond angle decreases by $\approx 4°$ in the $\tilde{A}$ state, thus explaining the observed vibrational progressions. Radiative lifetime measurements show a significant decrease for $\tilde{A}$ state vibrational levels $\geqslant 800\ cm^{-1}$ above the origin.[12,13,15,18] This effect, a likely signature of predissociation, limits LIF measurements to the region between $26\,200$–$28\,000\ cm^{-1}$, in contrast to low-resolution ultraviolet absorption measurements that show the $\tilde{A} \leftarrow \tilde{X}$ band extends to $31\,000\ cm^{-1}$.[19]

The methylthio radical has also been the subject of theoretical interest, motivated in part by the interactions between Jahn-Teller and spin–orbit effects in the degenerate $\tilde{X}\ ^2E$ ground state.[20] Several *ab initio* calculations have been performed to determine the energetics and geometry of the methylthio radical in its ground and excited electronic states.[8,21–23] Figure 1 shows the potential energy surfaces for the CH_3S radical along the C–S bond based upon the *ab initio* calculations of both Cui *et al.*[24] and Hsu *et al.*[22] The $\tilde{A}\ ^2A_1$ surface, which correlates asymptotically to excited state products $CH_3 + S(^1D)$, is crossed by three repulsive surfaces, the $^4A_2$, ^4E, and $^2A_2$ states. These correlate to ground state products $CH_3 + S(^3P_{2,1,0})$ and induce predissociation in the $\tilde{A}$ state. Recent *ab initio* studies by Cui and

[a]Current address: Institute of Physics and Astronomy, Univerisity of Aarhus, NY Munkegade, DK-8000 Aarhus C, Denmark.
[b]Current address: Coherent Inc., Medical Group, 2400 Condensa Street, Santa Clara, California 95051.

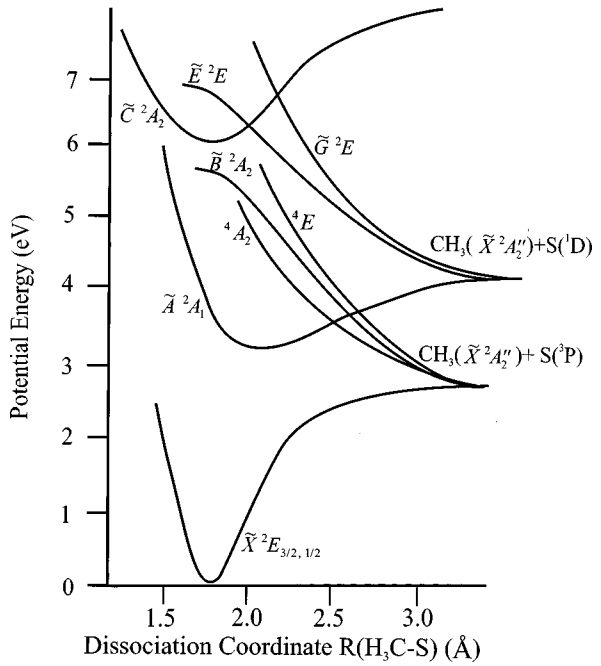

FIG. 1. Schematic C_{3v} potential energy surfaces for CH_3S along the C–S reaction coordinate based on calculations by Hsu *et al.* (Ref. 22) and Cui *et al.* (Ref. 24).

Morokuma[24] have focused on the predissociation of the $\tilde{A} \leftarrow \tilde{X}$ transitions for CH_3S, as well as the related species CH_3O, CF_3O, and CF_3S, calculating the minimum seams of crossing and spin–orbit coupling elements between the $\tilde{A}\ ^2A_1$ and the repulsive ^4E and $^4A_2$ states.

While most of the experimental and theoretical work has focused on the $\tilde{A} \leftarrow \tilde{X}$ band the photolysis of CH_3S has also been studied at higher photon energies. Hsu *et al.*[22] have examined the $S(^3P_{2,1,0};^1D)$ production from 193 nm photodissociation of CH_3S using a 2+1 resonance-enhanced multiphoton ionization technique, determining the $S(^3P)/S(^1D)$ ratio to be 0.15/0.85 and the fine-structure distribution for the $S(^3P_{2,1,0})$ levels to be nearly statistical. Wilson *et al.*[25] have studied the photodissociation of CH_3SH using the H-atom time-of-flight photodissociation spectroscopy observing $CH_3S(\tilde{X}\ ^2E)+H(^1S)$ as the major photodissociation products. Their results suggest that at 46 230 cm^{-1}, the CH_3S photofragment absorbs a second photon and dissociates to $H+CH_2S(\tilde{A}\ ^1A_2)$.

In the present study, a mass selected beam of CH_3S radicals is generated from laser photodetachment of CH_3S^- ions. A second laser is then used to probe the dissociative excited states of the methylthio radical. We report the first observation of several predissociative vibronic transitions of the $\tilde{A}\ ^2A_1 \leftarrow \tilde{X}\ ^2E$ electronic band and also observe dissociation from an unstructured band at 45 600 cm^{-1} that corresponds to the band originally observed by Callear and Dickson.[5] The primary photodissociation products were found to be $CH_3(\tilde{X}\ ^2A_2'')+S(^3P_j)$ for all photodissociation energies, although the detection scheme employed in these experiments in relatively insensitive to hydrogen loss channels (i.e., CH_2S+H). Photofragment translational energy and angular distributions reveal resolved vibrational product state distributions of the CH_3 fragment as well as fine-structure distributions for the $S(^3P_j)$ fragment. The experimental results and data analysis are presented in Secs. III and IV. Based on our results, we discuss the involvement of the $^4A_2$ and ^4E states in the predissociation of the $\tilde{A}$ state, and propose that photodissociation at 219.3 nm occurs along the more highly excited $\tilde{B}\ ^2A_2$ surface.

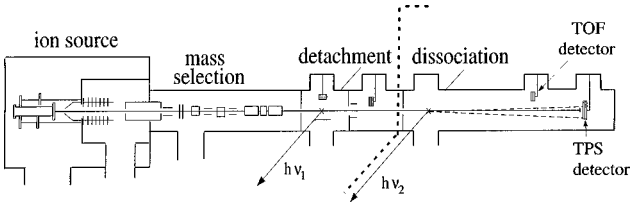

FIG. 2. Fast radical beam translational spectrometer. The dotted line separates the radical production section on the left from the actual photodissociation experiment on the right.

II. EXPERIMENT

The fast beam photofragment translational spectrometer, Fig. 2, has been described in detail elsewhere,[26–28] only a brief description will follow. In this experiment, a clean source of neutral radicals is generated by mass-selective laser photodetachment of a beam of negative ions. The neutral radicals are then photodissociated by a second laser,

$$CH_3S^- \xrightarrow{h\nu_1} CH_3S + e^- \xrightarrow{h\nu_2} CH_3 + S. \quad (1)$$

Methylthio anions are generated from a pulsed supersonic expansion of 800 mTorr of dimethyl disulfide (CH_3SSCH_3) seeded in 3 atm of Ar. For d_3-methylthio anions, d_6-dimethyl sulfide (CD_3SCD_3) is used as the precursor. The molecular beam immediately passes through a pulsed electric discharge. This generates negative ions, which are cooled both rotationally and vibrationally.[29] The ions are accelerated to a laboratory beam energy that can be varied from 6000 to 9000 eV and are mass selected using the Bakker time-of-flight (TOF) method,[30,31] resulting in ion packets with very low energy spread. An excimer-pumped pulsed dye laser then intersects the ion beam at the appropriate time so as to selectively photodetach the methylthio anions. Undetached anions are deflected from the beam by a pulsed electric field. Based upon electron affinities determined in previous photodetachment measurements,[6–8] a photodetachment energy of 1.93 eV was chosen to produce vibrationally and rotationally cold CH_3S radicals in the $^2E_{3/2}$ and $^2E_{1/2}$ states. The photodetachment energy was lowered to 1.88 eV when it was desired to produce CH_3S radicals in the $^2E_{3/2}$ state exclusively. For the production of d_3-methylthio radicals, photon energies of 1.92 eV and 1.87 eV were used.[8]

In the dissociation region, a second excimer-pumped pulsed dye laser intersects the methylthio radicals. The fragments from photodissociation of the radical are detected directly by one of two microchannel plate detector assemblies. An aluminum blocking strip is positioned at the center of

each detector to prohibit any undissociated radicals from impacting the detector, so the signal is entirely from recoiling photofragments. In the present experiments, the fundamental output of the dye laser with a bandwidth of 0.3 cm^{-1} was used between 27 000–29 800 cm^{-1}. The dye laser was frequency-doubled to produce photon energies between 29 500–32 300 cm^{-1} and 45 045–46 730 cm^{-1} with bandwidths of 0.4 cm^{-1} and 0.5 cm^{-1}, respectively.

Two types of experiments are performed. First, the spectroscopy of the dissociative electronic states is examined by measuring the total flux of photofragments arriving at the TOF detector, located 0.68 m from the dissociation laser, as a function of laser photon energy. The resulting photofragment yield (PFY) spectra are complementary to absorption and fluorescence measurements.

Once the spectroscopy of the dissociative states has been examined, the dissociation dynamics are probed using a coincidence detection scheme. Both photofragments from a single parent radical are detected in coincidence using a time-and-position sensitive detector based on the design of de Brujin and Los.[32] Our implementation of this detection scheme has been described in detail elsewhere.[26,27] The detector records the positions and difference in arrival time of the two photofragments from a single dissociation event. This information is then used to determine the masses of the fragments, their relative translational energy E_T, and the scattering angle θ between the relative velocity vector and the electric vector of the polarized dissociation laser (perpendicular to the ion beam axis),

$$\frac{m_1}{m_2}=\frac{r_1}{r_2}\left(1-\frac{v_0\tau}{L}\right), \tag{2}$$

$$E_T=E_0\cdot\frac{m_1m_2}{M}\cdot\frac{\{(v_0\tau)^2+R^2\}}{L^2}\left(1+2\frac{m_1-m_2}{M}\frac{v_0\tau}{L}\right), \tag{3}$$

$$\theta=\arctan\left(\frac{v_0\tau}{R}\right). \tag{4}$$

Here, r_1 and r_2 are the distances of each photofragment on the detector face to the center of the radical beam. $R=r_1+r_2$ is the distance between the two photofragments and τ is the difference in arrival time of the fragments. M, m_1, and m_2 are the masses of the parent radical and photofragments, respectively. E_0 and v_0 are the radical beam energy and velocity respectively and L is the distance from the dissociation laser to the detector face. A flight distance of 2(1) m was used for photoexcitation energies less (greater) than 30 000 cm^{-1}. The photofragment mass resolution is $m/\Delta m \approx 10$ while the translational energy resolution for these experiments is $\Delta E_T/E_T=3.0\%$ and 2.2% for data recorded at 1 and 2 m flight lengths, respectively. This coincidence detection scheme is only possible when the mass ratio of the two photofragments $m_1/m_2 \leqslant 4$, making coincident detection of light atom dissociation channels involving H or D impossible.

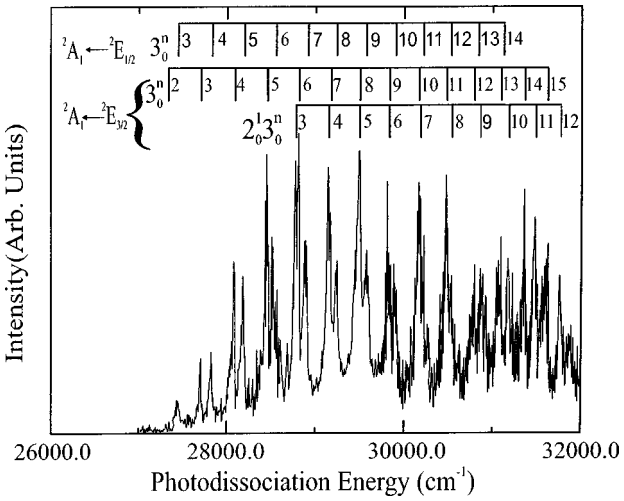

FIG. 3. Photofragment yield spectrum for the $\tilde{A}\leftarrow\tilde{X}$ band of CH_3S.

III. RESULTS

A. Photofragment yield spectra, $\tilde{A}\ ^2A_1\leftarrow\tilde{X}\ ^2E$ band

Figure 3 shows the PFY signal for the $\tilde{A}\ ^2A_1 \leftarrow\tilde{X}\ ^2E_{3/2,1/2}$ band system of CH_3S. The spectrum is highly structured with the first distinct peak occurring at 27 324 cm^{-1}. The transition frequencies and vibrational assignments are listed in Table I. The PFY spectra clearly extend to considerably higher energy than the LIF measurements, which were limited to transitions below 28 010 cm^{-1}, illustrating the competition between predissociation and fluorescence in the $\tilde{A}\ ^2A_1$ state. The observed vibrational progressions can be assigned in a relatively straightforward manner using the

TABLE I. Observed transitions, lifetimes, and assignments for the CH_3S $\tilde{A}\ ^2A_1\leftarrow\tilde{X}\ ^2E$ photofragment yield spectrum.

Transition energy (cm^{-1})			
$\tilde{A}\ ^2A_1\leftarrow\tilde{X}\ ^2E_{3/2}$	$\tilde{A}\ ^2A_1\leftarrow\tilde{X}\ ^2E_{1/2}$	Assignment	Lifetime (ns)
27321.3,[a] 27323.2	27062.2[a]	3_0^2	250±20[a]
27707.1,[a] 27708.2	27447.5	3_0^3	72±30[a]
28082.3	27824.1	3_0^4	0.025±0.025
28450.7	28186.2	3_0^5	0.010±0.007
28780.5		$2_0^1 3_0^3$	0.025±0.025
28810.3	28536.3	3_0^6	0.004±0.002
29144.3		$2_0^1 3_0^4$	0.008±0.005
29176.5	28998.7	3_0^7	0.002±0.002
29498.7	29241.1	3_0^8, $2_0^1 3_0^5$	
29817.4	29580.7	3_0^9, $2_0^1 3_0^6$	
30162.4	29889.6	3_0^{10}, $2_0^1 3_0^7$	
30479.8	30221.1	3_0^{11}	0.002±0.002
30523.5	30265.7	$2_0^1 3_0^8$	
30787.7	30527.8	3_0^{12}	
30626.6		$2_0^1 3_0^9$	
31088.0		3_0^{13}	
31171.9	30910.3	$2_0^1 3_0^{10}$	
31375.6		3_0^{14}	
31479.8		$2_0^1 3_0^{11}$	
31641.5		3_0^{15}	
31762.6		$2_0^1 3_0^{12}$	

[a]Transitions and lifetimes observed in Ref. 15.

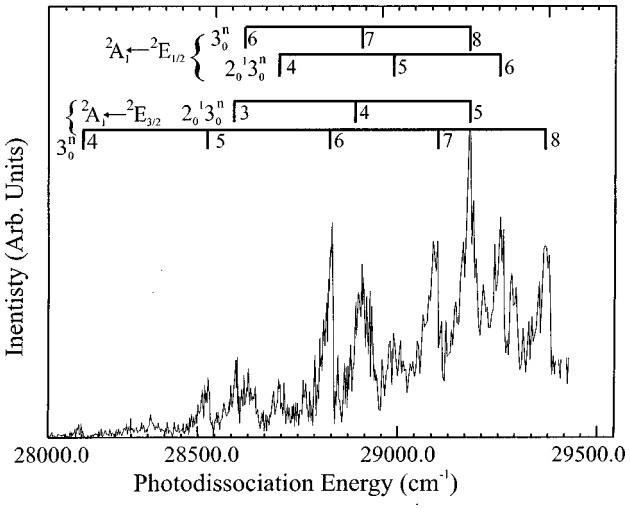

FIG. 4. Photofragment yield spectrum for the $\tilde{A}\leftarrow\tilde{X}$ band of CD_3S.

previously determined vibrational frequencies and anharmonicities from LIF measurements.[15–17] All progressions show a spacing of approximately 390 cm^{-1}, characteristic of excitation in the ν_3 C–S stretching mode. Two of these progressions are separated by approximately 260 cm^{-1}, the spin–orbit splitting of CH_3S in the $\tilde{X}\ ^2E$ state, and are assigned to 3_0^n progression from the $^2E_{3/2}$ and $^2E_{1/2}$ states. Transitions from the $^2E_{3/2}$ level are approximately twice as intense as transitions from the $^2E_{1/2}$, due to the larger cross section for photodetachment of CH_3S^- to the (lower) $^2E_{3/2}$ state at 1.93 eV. A third progression begins at 28 780 cm^{-1}, approximately 1080 cm^{-1} above the $3_0^3(^2E_{3/2})$ transition. Based on the excited state ν_2 umbrella mode frequency of 1096 cm^{-1},[15] this band is assigned to the $2_0^1 3_0^n(^2E_{3/2})$ progression with $n\geqslant 3$. A number of $2_0^1 3_0^n(^2E_{1/2})$ transitions are resolved and are indicated in Table I.

Rotational resolution of the vibrational features of the PFY spectra was not attempted due to spectral congestion resulting from multiple K stacks and a low rotational constant $B'=0.345\ cm^{-1}$. The peaks of the PFY spectra are approximately 20 cm^{-1} FWHM with a tail extending to lower photon energy. The vibrational bands, scanned with laser step size of 2.5 cm^{-1} and bandwidth of 0.3 cm^{-1}, do not show significant broadening with increased excitation energy. The rotational temperatures of the vibrational peaks have been determined by fitting the peaks to a rotational contour using the rotational constants for the vibrationless level of the $\tilde{A}$ state determined by Miller and co-workers.[14] These contours yield rotational temperatures between 40–50 K.

A PFY spectrum has also been obtained for the $\tilde{A}\leftarrow\tilde{X}$ band of CD_3S, shown in Fig. 4. The structure in CD_3S PFY spectrum is not as well resolved as in the corresponding CH_3S spectra because the ion beam intensity was approximately half that for CH_3S^-. Four major progressions are observed with a spacing of approximately 370 cm^{-1} and significant anharmonicity. By applying the vibrational frequencies and anharmonicities from previous LIF measurements,[16] these progressions can be assigned to 3_0^n and $2_0^1 3_0^n$ bands

TABLE II. Observed transitions, lifetimes, and assignments for the CH_3S $\tilde{A}\ ^2A_1\leftarrow\tilde{X}\ ^2E$ photofragment yield spectrum.

Transition energy (cm^{-1})		
$\tilde{A}\ ^2A_1\leftarrow\tilde{X}\ ^2E_{3/2}$	$\tilde{A}\ ^2A_1\leftarrow\tilde{X}\ ^2E_{1/2}$	Assignment
28089		3_0^4
28470		3_0^5
28564		$2_0^1 3_0^3$
28849	28601	3_0^6
28940	28693	$2_0^1 3_0^4$
29156	28967	3_0^7
29262	29036	$2_0^1 3_0^5$
29492	29036	3_0^8
	29357	$2_0^1 3_0^6$

from the $E_{3/2}$ and $E_{1/2}$ states with a spin–orbit splitting of about 250 cm^{-1}. The transition frequencies and vibrational assignments are listed in Table II.

B. Translational energy distributions, $\tilde{A}\ ^2A_1\leftarrow\tilde{X}\ ^2E$ band

The possible reaction pathways for the methylthio radical for excitation energies in the $\tilde{A}\leftarrow\tilde{X}$ band are

$$CH_3S(\tilde{X}\ ^2E)\xrightarrow{h\nu}$$

$$CH_3(\tilde{X}\ ^2A_2'')+S(^3P_{2,1,0}) \quad \Delta H_{rxn,0}=3.045\pm 0.015\ \text{eV} \tag{I}$$

$$CH_2S(\tilde{X}\ ^1A_1)+H(^2S) \quad \Delta H_{rxn,0}=2.06\pm 0.08\ \text{eV}. \tag{II}$$

These reaction energies were calculated using the JANAF Thermochemical Tables[33] and $\Delta H_{f,0}(CH_3S)=1.346\pm 0.018$ eV, determined in this work (see below). Our coincident detection scheme is insensitive to the H-atom dissociation channels as has been discussed by Osborn *et al.*,[28] making channel I the only detectable photodissociation pathway.

The two-dimensional coupled translational energy distribution, $P(E_T,\theta)$, obtained from Eqs. (3) and (4) can be separated into the angle-independent translational energy distribution $P(E_T)$ and the energy-dependent anisotropy parameter $\beta(E_T)$ which describes the angular distribution of the fragments[34]

$$P(E_T,\theta)=P(E_T)[1+\beta(E_T)P_2(\cos\ \theta)]. \tag{5}$$

The anisotropy parameter β can range from $+2$ to -1, corresponding to $\cos^2\theta$ and $\sin^2\theta$ angular distributions, respectively.

Figure 5 shows the translational energy distributions, $P(E_T)$, for a number of vibrational transitions associated with the $\tilde{A}\ ^2A_1\leftarrow\tilde{X}\ ^2E$ band of CH_3S. The mass ratio, $m_1:m_2=15:32$, determined via Eq. (2), confirms CH_3+S as the product channel. The structure observed in the $P(E_T)$ distributions can be attributed to the $S(^3P_{2,1,0})$ levels and the umbrella motion of the CH_3 fragment, as indicated in Fig. 5 for the 3_0^7 transition with two combs representing the maximum translational energies for the $S(^3P_j)$ fine-structure states for the $\nu_2=0$ and $\nu_2=1$ vibrational states of the CH_3 fragment. The detailed assignment of this structure is de-

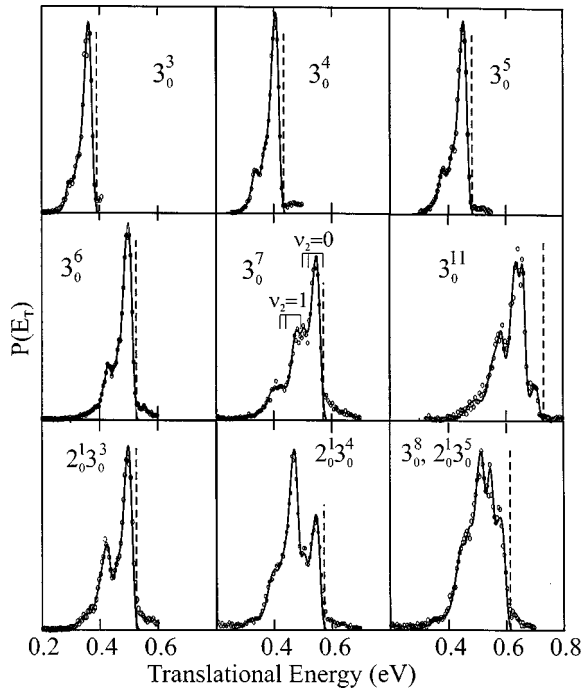

FIG. 5. $P(E_T)$ distributions for $\tilde{A}\leftarrow\tilde{X}$ vibrational transitions of CH_3S. The experimental data is indicated by the open circles. The fit (—) and $E_T^{\max}$ values (— — —) are shown for each $P(E_T)$ distribution. The combs shown for the 3_0^7 transition represent the maximum translational energies for the three fine-structure states of the $S(^3P_j)$ fragment that correspond to the $\nu_2=0$ and $\nu_2=1$ vibrational states of the CH_3 fragment.

scribed in Sec. IV. The dashed vertical lines at each excitation energy in Fig. 5 indicate $E_T^{\max}$, the maximum translational energy available, as determined below in Sec. IV.

The $P(E_T)$ distributions for 3_0^n excitations for $n=3-6$ are dominated by single narrow peaks with a sharp cutoff at $E_T^{\max}$, displaying little or no vibrational and/or spin–orbit excitation. The $3_0^7 P(E_T)$ distribution shows a mild increase in the internal excitation of the photofragments, and the $3_0^{11} P(E_T)$ distribution demonstrates a significant increase in photofragment excitation, with a maximum in the $P(E_T)$ distribution at a translational energy 70 meV less than the maximum translational energy.

The $P(E_T)$ distributions for the $2_0^1 3_0^n$ transitions are quite different. The photon energies used to acquire the $P(E_T)$ distributions for the $2_0^1 3_0^n$ transitions differ from the 3_0^{n+3} transitions by only 25 and 22 cm^{-1}, for $n=3$ and 4, respectively, but the combination band transitions produce significantly more internal excitation in the photofragments. The $P(E_T)$ distribution from the overlapping $2_0^1 3_0^5$ and 3_0^8 bands is not well resolved, as one might expect for a combination of two different product state distributions. Due to the overlapping combination band and C–S stretch progressions between 29 400–30 100 cm^{-1} as well as low signal levels, no attempt was made to measure the dissociation dynamics of the 3_0^{n+3} or $2_0^1 3_0^n$ bands for $n=6$ and 7.

The photofragment angular distributions are highly anisotropic with values of β ranging between -0.2 to -1.0, with a decrease in β as the C–S stretch quantum number is increased, see Fig. 9. The negative β values are consistent with a perpendicular $A\leftarrow E$ transition dipole moment.

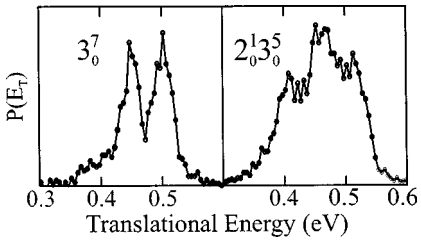

FIG. 6. $P(E_T)$ distributions for the 3_0^7 and $2_0^1 3_0^5$ transitions fr CD_3S.

The smaller ion beam intensities for CD_3S resulted in reduced signal collection rates, and $P(E_T)$ distributions were obtained at only two photon energies, 29 150 and 29 260 cm^{-1}, Fig. 6. These transitions produce photofragments with a mass ratio of 18:32, consistent with CD_3+S products. Photoexcitation at 29 260 cm^{-1}, which overlaps the $2_0^1 3_0^5(E_{3/2})$ and $3_0^8(E_{1/2})$ transitions, leads to substantially more internal excitation of the photofragments than the nearby $3_0^7(E_{3/2})$ transition at 29 150 cm^{-1}. The photofragment angular distributions are described by $\beta=-0.3$ and -0.1 for the 3_0^7 and $2_0^1 3_0^5$ bands, respectively.

C. Higher excitation energies

A PFY spectra has also been obtained for CH_3S between 45 000–46 500 cm^{-1}, Fig. 7, corresponding to the UV absorption band observed originally by Callear and Dickson[5] and in more recent experiments.[19,35] Our experiment confirms that CH_3S is the carrier of this band. The peaks at 45 620 and 45 350 cm^{-1} do not correspond to vibronic structure, but to transitions from the $^2E_{3/2}$ and $^2E_{1/2}$ states, respectively. The relative intensity of the peaks is governed by the larger detachment cross section to the $^2E_{3/2}$ state at 1.93 eV.[8] The peak at 45 350 cm^{-1} disappears when the detachment energy is lowered to 1.87 eV.

The photofragment mass ratio for excitation at 45 620 cm^{-1} was found to be 15:32, consistent with CH_3+S products. The $P(E_T)$ distribution, Fig. 8, peaks at 2.40 eV, near

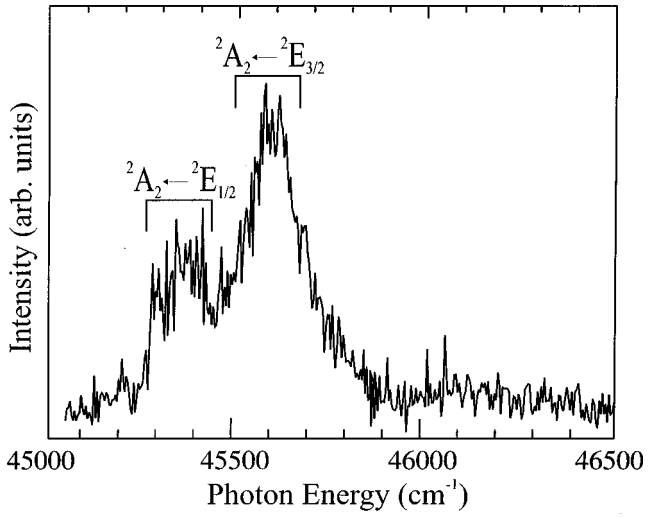

FIG. 7. Photofragment yield spectrum for CH_3S from 45 000 to 46 500 cm^{-1}. The peaks at 45 620 and 45 350 cm^{-1} are assigned to transitions arising from the $\tilde{X}\ E_{3/2}$ and $\tilde{X}\ E_{1/2}$ states, respectively.

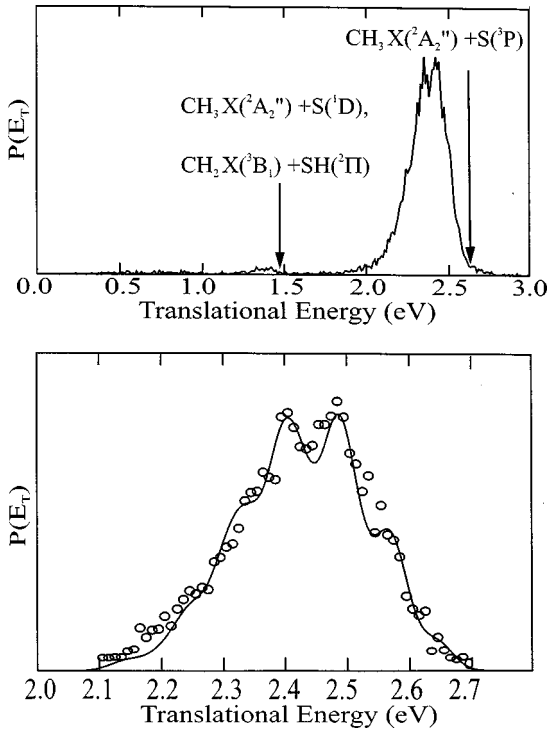

FIG. 8. (a) $P(E_T)$ distribution from excitation at 45 620 cm^{-1}. The maximum translational energies for the $CH_3+S(^3P)$, $CH_3+S(^1D)$, and $CH_2+SH(^2\Pi)$ are marked with arrows. (b) $P(E_T)$ between 2.0 and 2.8 eV. The experimental data are displayed as open circles while the results of an impulsive dissociation model is shown with the solid (—) line.

the maximum allowable translational energy of 2.6 eV for product channel I. This distribution is structured, but much less so than the $P(E_T)$ distributions for the $\tilde{A}\leftarrow\tilde{X}$ transitions. The small feature at $E_T=1.5$ eV comprises ≈2% of the photodissociation products and is most likely from dissociation channels III or IV,

$$CH_3(\tilde{X}(^2A_2''))+S(^1D) \quad \Delta H_{rxn,0}=4.190\pm0.015, \qquad \text{(III)}$$

$$CH_2(\tilde{X}(^3B_1''))+SH(^2\Pi), \quad \Delta H_{rxn,0}=4.14\pm0.05. \qquad \text{(IV)}$$

The photofragment angular distribution is highly anisotropic with $\beta=-0.98\pm0.10$.

Attempts to determine the relative branching ratios of the H-atom vs S-atom channels at 45 620 cm^{-1} through the use of a noncoincident time-of-flight technique[28] were unsuccessful. Our ability to detect the H-atom dissociation products $H(^1S)+CH_2S(\tilde{A}\ ^1A_2)$ observed by Wilson *et al.* at 216.3 nm (Ref. 25) is extremely limited by our detector geometry. The H-atom detection efficiency is ≤1% and only a small fraction (<10%) of $CH_2S(\tilde{A}\ ^1A_1)$ fragments are expected to contain sufficient kinetic energy to clear the 3 mm beam block used to prevent undissociated neutrals from impacting the detector.

IV. ANALYSIS

A. CH_3S photofragment yield spectra, $\tilde{A}\ ^2A_1\leftarrow\tilde{X}\ ^2E$ band

Our photofragment yield experiments are the first to present resolved vibrational transitions of $\tilde{A}\leftarrow\tilde{X}$ band with more than three quanta in the ν_3 mode, showing an extended 3_0^n progression containing up to 15 quanta and a $2_0^1 3_0^n$ combination band progression. These progressions are consistent with the large change in the C–S bond length upon excitation to the $\tilde{A}$ state (1.767 Å–2.057 Å).[14] Our observed frequencies for the 3_0^2 and $3_0^3 E_{3/2}$ transitions for CH_3S agree to within ±2 cm^{-1} with those observed in previous LIF studies.[15,17] The 3_0^n progressions, $n=2-15$, can be fit effectively using with the frequency, $\omega_3'=409.2\pm0.2$ cm^{-1}, and anharmonicity, $x_{33}'=3.9\pm0.1$ cm^{-1}, from Chiang *et al.*[15] The combination band progression, $2_0^1 3_0^n$, can be fit by including an additional term $x_{23}'=6.6\pm0.1$ cm^{-1}, from Chiang *et al.*[15] to describe the interaction of the ν_2 and ν_3 mode.

Previous fluorescence lifetime measurements reveal a sharp decrease in the lifetime of the excited state for the 3_0^2 transition (250±20 ns) relative to the 0_0^0 transition (1130±70 ns), suggesting the former to be the onset of predissociation.[12,15,18] The PFY spectra obtained in this study indeed shows the 3_0^2 transition to be the first dissociative transition. The most energetic peaks observed via LIF are the 3_0^3 and $2_0^1 3_0^1$ transitions, with lifetimes of 72±30 ns and 85±15 ns, respectively. While we do observe the 3_0^3 transition, we are not able to detect the $2_0^1 3_0^1$ transition at 28 016 cm^{-1} even though the reported lifetime of 85±15 ns suggests rapid predissociation. Although extensive efforts were made to observe both the $2_0^1 3_0^1$ and $2_0^1 3_0^2$ bands, the combination bands $2_0^1 3_0^n$ were not clearly observed until $n\geqslant3$.

B. CD_3S photofragment yield spectra

The CD_3S photofragment yield spectrum is also comprised of 3_0^n and $2_0^1 3_0^n$ progressions. The 3_0^n transitions from the current PFY spectra and LIF transitions found by Suzuki *et al.*[16] can be fit using $\omega_3'=402.5\pm1.0$ cm^{-1} and $x_{33}'=4.15\pm0.2$ cm^{-1}. The combination bands can be fit by including a cross anharmonicity x_{23}' of 4.0±0.5 cm^{-1}.

Radiative lifetime measurements of Suzuki *et al.* suggest the onset of predissociation occurs at the 3_0^3 transition. We have been unable to locate the 3_0^3 transition in our PFY experiments and do not observe significant dissociation signal until the 3_0^4 transition. Our inability to detect the 3_0^3 transition probably results from a combination of poor Franck–Condon factors and small ion beam intensities.

C. Translational energy distributions, $\tilde{A}\ ^2A_1\leftarrow\tilde{X}\ ^2E$ band

The $P(E_T)$ distributions in Fig. 5 demonstrate how the excess energy above the dissociation threshold is distributed between the photofragments. The energy balance for CH_3S photodissociation is described by

$$h\nu+E_{SO}(CH_3S)+E_{int}(CH_3S) = D_0(CH_3\text{–}S)+E_T+E_V(CH_3)+E_R(CH_3) + E_{SO}(S\ ^3P_j), \qquad (6)$$

where $h\nu$ is the photon energy, $E_{SO}(CH_3S)=0$ and 260 cm^{-1} for $^2E_{3/2}$ and $^2E_{1/2}$ states, respectively, of the parent radical and E_{int} characterizes the average rotational energy of the parent. E_T is the measured center-of-mass translational

TABLE III. Product branching ratio for $CH_3S \rightarrow CH_3(\nu_2=n)+S(^3P_j)$.

Transition	$h\nu$ (cm^{-1})	$\nu_2=0$			$\nu_2=1$			$\nu_2=2$			Fine-structure ratio
		$^3P_2$	$^3P_1$	$^3P_0$	$^3P_2$	$^3P_1$	$^3P_0$	$^3P_2$	$^3P_1$	$^3P_0$	$^3P_2$:$^3P_1$:$^3P_0$
3_0^3	27 705	87	5	4	3	1	⋯	⋯	⋯	⋯	90:6:5
3_0^4	28 082	82	6	6	6	⋯	⋯	⋯	⋯	⋯	88:6:6
3_0^5	28 450	79	6	5	10	1	⋯	⋯	⋯	⋯	89:7:5
3_0^6	28 810	76	6	4	11	2	1	⋯	⋯	⋯	87:8:5
3_0^7	29 160	53	15	4	13	5	5	4	⋯	1	70:20:10
3_0^{11}	30 479	7	27	31	4	12	10	4	3	2	15:42:43
$2_0^1 3_0^3$	28 780	61	5	1	29	⋯	2	2	⋯	⋯	90:5:5
$2_0^1 3_0^4$	29 134	29	11	3	39	7	4	5	1	1	73:19:8

energy, E_V and E_R are the CH_3 product vibrational and rotational energies, $E_{SO}(S\ ^3P_j)$ is the spin–orbit state of the sulfur atom, and $D_0(CH_3\text{–}S)$ is the C–S bond dissociation energy. $E_{int}(CH_3S)$ for a temperature of 50 K is 33 cm^{-1}.

$D_0(CH_3\text{–}S)$ can be extracted from these distributions if we can determine E_T^{max}, the value of the translational energy corresponding to production of photofragments with zero internal energy. This is marked by a vertical dashed line for each photon energy. Although E_T^{max} is not always obvious from a $P(E_T)$ distribution, it can be readily ascertained from the distributions in Fig. 5 because of the steep falloff in intensity toward high E_T. Note that the $P(E_T)$ distributions for the 3_0^6 and 3_0^7 transitions show broad tails which extend to higher translational energies than E_T^{max}. This ''signal'' arises when the dissociation cross section is large enough that photofragments from different dissociation events impact the detector. While our data analysis allows us to eliminate most of false coincidences, a small contribution remains when large photofragment fluxes as present.

$D_0(CH_3\text{–}S)$ is obtained independently at each photon energy; the resulting values are then averaged together to yield a value of 3.045 ± 0.015 eV. Our value of D_0 along with the known heats of formation of CH_3 and S determines $\Delta H_{f,0}(CH_3S)=1.346\pm0.018$ eV,[33] in good agreement with the value 1.363 ± 0.023 reported by Nicovich *et al.*[36] determined from reaction kinetic measurements and with theoretical values 1.346, and 1.37 eV.[23,37] Our current value disagrees with the values of 1.54 ± 0.086, 1.53 ± 0.065, and 1.48 ± 0.065 obtained by Nourbakhsh *et al.* from molecular beam photofragmentation studies of CH_3SH,[38] CH_3SSCH_3,[39] and CH_3SCH_3,[40] respectively. The discrepancy of this value with other recent literature values has been previously discussed by Ruscic and Berkowitz[41] and by Nicovich *et al.*[36]

The CH_3 product umbrella mode (ν_2) vibrational distribution and the $S(^3P_j)$ fine-structure distribution can also be determined from the $P(E_T)$ distributions. Since both photofragments are detected in coincidence, this is a correlated distribution in the sense that we obtain the $S(^3P_j)$ distribution for each CH_3 vibrational level. These distributions have been obtained by using a similar procedure to that employed by Osborn *et al.*[42] for CH_3O dissociation with additional terms included to account for the resolved fine-structure states of the sulfur atom. The data are fit to a series of rotational distribution functions separated by the fine-structure energy levels of the sulfur atom and the term energies for the CH_3 ν_2 umbrella mode.[43,44] The distribution functions $f_{j,n}(E_T)$, where j labels the sulfur atom fine-structure level and n labels the number of quanta in CH_3 ν_2 mode, are Boltzmann distributions described by a rotational temperature T (characteristic of the CH_3 fragment) and convoluted with a gaussian experimental energy resolution δ, FWHM=20 meV.

The total distribution is given by

$$F(E_T)=\sum_{j=0}^{2}\sum_{n=0}^{n'}\alpha_{j,n}f_{j,n}[E_T-(h\upsilon-n\omega_2-SO_j-D_0),T,\delta], \tag{7}$$

where ω_2 is the fundamental frequency of the ν_2 mode (606 cm^{-1}, 75 meV)[43,44], $\alpha_{j,n}$ represents the coefficient associated with each individual distribution function and SO_j is the internal energy associated with the $S(^3P_{2,1,0})$ spin–orbit levels, which have energies of 0, 49, and 71 meV,[33] respectively. The rotational temperature T was manually adjusted for each peak to produce the best fit. The results of the best nonlinear least squared fits are shown as solid lines in Fig. 5. Table III contains the vibrational and spin–orbit distribution for each data set. The rotational temperature of the CH_3 fragment varied between 170 to 220 K for all correlated product distributions except for the $CH_3+S(^3P_1)$ distributions for which the CH_3 fragment rotational temperatures varied from 50 to 100 K.

The fundamental frequency of the CH_3 umbrella mode, ν_2, is ≈75 meV which is very close to the energy splitting between the $S(^3P_2)$ and $S(^3P_0)$ levels ≈71 meV. This leads to product states, $CH_3(\nu_2=0)+S(^3P_2)$ and $CH_3(\nu_2=1)+S(^3P_0)$ which are nearly degenerate within the experimental resolution of 20 meV and cannot be distinguished by the fit. This near degeneracy is removed as the number of quanta in the strongly negatively anharmonic CH_3 umbrella mode is increased. For product state energies separated by more than 15 meV, the fits were sensitive to changes in the spin–orbit and vibrational state distributions of more than 5%. The uncertainty in the product state distributions for products $CH_3(\nu_2=0)+S(^3P_2)$ and $CH_3(\nu_2=1)+S(^3P_0)$ could not be determined.

The $P(E_T)$ distributions from $3_0^n(n\leqslant 6)$ transitions are remarkably similar with at least 86% of the CH_3 produced in the $\nu_2=0$ state. These transitions also exhibit a strong pref-

erence for the $S(^3P_2)$ level with an average $S(^3P_{2:1:0})$ distribution of 88:7:5 compared to a statistical distribution of 5:3:1. However, these trends change for $n>6$. The 3_0^7 transition has a spin–orbit distribution of approximately 73:18:7, showing an increase in the higher energy $^3P_1$ and $^3P_0$ levels. This transition also shows increased vibrational excitation with a vibrational distribution $\nu_2=0:1:2$ of 72:23:5. The 3_0^{11} transition is dramatically different from the other 3_0^n transitions in Fig. 5 showing a spin–orbit distribution of $S(^3P_{2:1:0})$ of 15:42:43 and a vibrational distribution $\nu_2=0:1:2$ of 65:26:9.

Excitation of the $2_0^1 3_0^n$ combination band transitions produces $P(E_T)$ distributions with a substantial increase in the excitation of the CH_3 product umbrella mode, e.g., $CH_3(\nu_2=1)$ is the dominant channel from excitation of the $2_0^1 3_0^4$ transition. Since the dissociation products, $CH_3(\nu_2=0)+S(^3P_0)$ and $CH_3(\nu_2=1)+S(^3P_2)$, cannot be distinguished by the fit, it was assumed that the spin–orbit distributions for the $2_0^1 3_0^n$ transitions were the same as for the nearly isoenergetic 3_0^{n+3} transitions. The spin–orbit distributions were then adjusted slightly to see if a better fit could be produced.

D. Excited state lifetimes

Due to spectral congestion of rotational levels in our experiment, we were unable to obtain rotationally resolve the transitions of the $\tilde{A}\leftarrow\tilde{X}$ band and therefore could not determine the excited state lifetime from linewidth measurements. We have therefore attempted to extract the excited state lifetimes from the anisotropic photofragment angular distributions and a defined excited state rotational distribution in a manner similar to that performed by Black *et al.*[45] in their study of ICN photodissociation. The anisotropy parameter β can be described classically as

$$\beta=2\cdot P_2(\cos\chi)g(\omega,\tau), \tag{8}$$

where P_2 is the second Legendre polynomial, χ is the orientation of the transition dipole moment with respect to the molecular axis ($\chi=90°$ for a perpendicular transition) and $g(\omega,\tau)$ describes the effect of molecular rotation on the photofragment angular distribution with a given dissociation lifetime τ.[46–48] The angular velocity of the separating fragments is given by ω.

For a diatomic molecule,

$$g(\omega,\tau)=\frac{1+(\omega\tau)^2}{1+4(\omega\tau)^2}. \tag{9}$$

Equation (12) describes the dependence of angular velocity upon the rotational quantum number J,

$$\omega(J)=\frac{BcJ(J+1)}{2\pi}, \tag{10}$$

where B is the rotational constant of the $\tilde{A}$ state, and c is the speed of light. The anisotropy parameter as a function of lifetime, $\beta(\tau)$, is then given by,

$$\beta(\tau)=2\cdot P_2(\cos\chi)\sum_J c_J\cdot\left(\frac{1+\omega(J)\cdot\tau^2}{1+4\omega(J)\cdot\tau^2}\right), \tag{11}$$

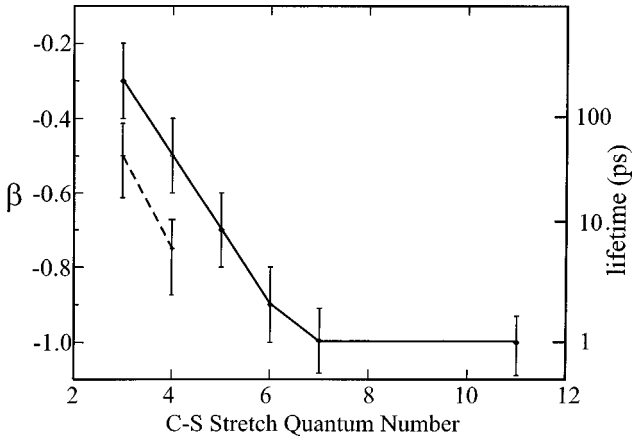

FIG. 9. Dependence of the anisotropy parameter, β, as a function of C–S stretch quantum number for the 3_0^n progression (—) and the $2_0^1 3_0^n$ progression (— — —). Error bars of ±0.1, for the uncertainty in the experimental value of β are shown.

where c_J is the fractional population for each rotational quantum number, J. The experimental value of β can then be associated with a lifetime.

Equation (9) applies to diatomic molecules and to symmetric top rotational levels with $K=0$. In our experiment, the excitation energies correspond to $K'=0\leftarrow K''=1$ transitions; the upper state $(J',K'=0)$ levels can then be considered as pseudodiatomic rotational levels, so that Eq. (9) is appropriate. We note that these are the most prominent transitions between K levels; most of the CH_3S $\tilde{X}\,^2E$ population is in rotational levels with $K''=1$, and for $a-e$ type vibronic transitions, $\Delta K=-1$ transitions are most intense.[49–51]

A cursory inspection of Eqs. (8)–(11) reveals that the upper state rotational distribution is required in this analysis. Although individual rotational lines are not resolved, it is assumed that the excited state contains discrete rotational levels and that the excitation laser with a bandwidth of ≈0.3 cm^{-1} selects a narrow distribution of rotational levels. The excited state rotational distribution is determined by first fitting the contour of each vibronic transition using the known rotational parameters of the $\tilde{X}$ and $\tilde{A}$ states,[9,14] a laser resolution of 0.3 cm^{-1} and then considering which part of the rotational manifold is excited for each $P(E_T)$ measurement.

The β parameter dependence upon C–S stretch excitation is plotted in Fig. 9 for both 3_0^n and $2_0^1 3_0^n$ transitions with the corresponding lifetimes and uncertainties listed in Table I, clearly illustrating the rapid decrease in β and in lifetime with increasing C–S stretch excitation. The uncertainty in the lifetime increases substantially as the photofragment anisotropy approaches its limiting classical value of −0.25 making the lifetimes for nearly isotropic distributions such as the 3_0^3 and 3_0^4 transitions less reliable. While the extracted lifetime values are only approximate, they agree surprisingly well with the lifetime values of the $\tilde{A}\leftarrow\tilde{X}$ band of the CF_3S radical reported by Powers *et al.*[52] A more detailed comparison of the CH_3S and CF_3S radicals and their excited state lifetimes will be provided in Sec. V.

V. DISCUSSION

A. Translational energy distributions, $\tilde{A}\ ^2A_1 \leftarrow \tilde{X}\ ^2E$

1. Vibrational state distributions

The product state distributions from photodissociation provide detailed information about the electronic surfaces which mediate dissociation. In this and the following section, we discuss how the product vibrational and fine-structure distributions provide insight into the role of the three repulsive surfaces in the predissociation of the $\tilde{A}$ state.

The $P(E_T)$ distributions for the $\tilde{A} \leftarrow \tilde{X}\ 3_0^n (n \leqslant 6)$ transitions show negligible excitation of the umbrella mode in the CH_3 fragment with a slight increase in $\langle E_{\rm vib} \rangle$ as n increases from 3 to 6. $\langle E_{\rm vib} \rangle$ rises noticeably for the 3_0^7 transition even more so for the 3_0^{11} transition, suggesting that a fundamental change in the dissociation dynamics occurs over this energy range. Cui and Morokuma[24] have performed detailed *ab initio* calculations for the predissociative surfaces of the methoxy family (CH_3O, CH_3S, CF_3O, and CF_3S). In particular, these authors have analyzed how fast the H–C–O bond angle opens in CH_3O as the C–O bond breaks on both the $^4A_2$ and ^4E surfaces. They find that the H–C–O bond angle opens more quickly as the C–O bond distance increases on the ^4E surface than on the $^4A_2$ surface. The resulting higher curvature along the minimum energy path on the ^4E surface promotes increased vibrational excitation of the CH_3 photofragment at higher photon energies as observed by Osborn *et al.*[53] Assuming that the same trend holds for CH_3S, the increased CH_3 product vibrational excitation observed for the 3_0^7 and 3_0^{11} transitions is consistent with involvement of the ^4E surface in the dissociation. No calculations of this type were performed for the $^2A_2$ state, so one cannot assess the role of this state based on the vibrational distributions alone.

The $2_0^1 3_0^3$ and $2_0^1 3_0^4$ transitions result in more vibrational excitation of the CH_3 photofragment as compared to the 3_0^n bands, with initial excitation of the CH_3S parent umbrella mode leading to population of the umbrella mode in the CH_3 fragment. While this result is not entirely surprising, the $2_0^1 3_0^4$ results in significantly more vibrational excitation of the CH_3 fragment than the $2_0^1 3_0^3$ transition, with the vibrational distribution peaking at $\nu_2 = 1$. This suggests that the upper level of the $2_0^1 3_0^4$ transition is also predissociated by the ^4E surface. Note that the $2_0^1 3_0^4$ transition is at nearly the same energy as the 3_0^7 transition, the first member of the 3_0^n progression in which the ^4E state appears to play a role.

2. Fine-structure distributions

The experimentally observed sulfur atom $S(^3P_j)$ fine-structure distributions yield further insight into the dissociative electronic states. In this section we compare the predicted fine-structure distributions for an adiabatic dissociation model for the repulsive $^4A_2$, $^2A_2$, and ^4E states to the experimentally observed fine-structure distributions. For simplicity, CH_3S will be regarded as a pseudodiatomic. The $\tilde{A}\ ^2A_1$ state has angular momentum values $\Lambda = 0$, $\Sigma = 1/2$, and $\Omega = 1/2$ where Λ, Σ, and Ω refer to the electronic, spin, and total angular momentum along the C–S axis, respectively. The $\tilde{A}\ ^2A_1$ state can couple to the repulsive $^4A_2$, $^2A_2$, and ^4E states via a spin–orbit interaction. Because of the spin–orbit coupling selection rules, $\Delta\Omega = 0$, $\Delta\Sigma = -\Delta\Lambda = \pm 1$, or $\Delta\Sigma = \Delta\Lambda = 0$,[54] we need only consider the $\Omega = 1/2$ states $^4A_{2(\Omega=1/2)}$, $^2A_{2(\Omega=1/2)}$, $^4E_{(\Omega=1/2)}$ states in our dissociation model.

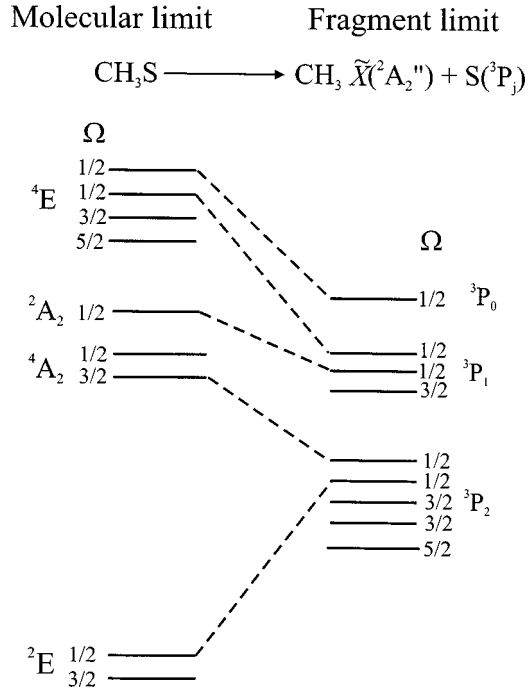

FIG. 10. Adiabatic correlation diagram for CH_3S to products $CH_3 + S(^3P_j)$ for the $\Omega = 1/2$ levels based upon calculations of Cui *et al.* (Ref. 24).

In the relativistic adiabatic limit, the nuclei evolve slowly on relativistic adiabatic potentials all the way to the asymptotic products.[27,54] Adiabatic curves with the same value of Ω will undergo avoided crossings, so a one-to-one mapping between the molecular electronic states and the asymptotic fine-structure states can be performed. In the dissociation limit, Ω is defined as the projection of the total electronic angular momentum vector (spin+orbital) of the separated atoms along the internuclear axis. Following the calculations of Cui and Morokuma,[24] we have constructed an adiabatic correlation diagram, Fig. 10, for the $\Omega = 1/2$ levels of CH_3S. This diagram shows that the $^4A_{2(\Omega=1/2)}$ state correlates with the $^3P_2$ products, the $^2A_{2(\Omega=1/2)}$ state correlates with $^3P_1$ products, and the $^4E_{1/2}$ states correlate with both $^3P_1$ and $^3P_0$ products.

Comparison of Table III with Fig. 10 shows that for energies below the 3_0^7 and $2_0^1 3_0^4$ transitions (i.e., photon energies $\leqslant 29\,000$ cm^{-1} for transitions originating from the $^2E_{3/2}$ state), the average distribution of 88:6:6 agrees relatively well with adiabatic dissociation on the $^4A_2$ state, which should yield $^3P_2$ products exclusively. At higher energies, the spin–orbit distribution changes abruptly and exhibits an increased fraction of the $^3P_1$ and $^3P_0$ states, with these states dominating the $P(E_T)$ distribution for the 3_0^{11} transition, $S(^3P_{2:1:0}) = 14{:}39{:}46$. The spin–orbit distribution for the 3_0^7 transition of 70:20:10 suggests that while dissociation on the $^4A_2$ surface dominates, some dissociation also occurs on both the $^2A_2$ and ^4E states. For the 3_0^{11} transition,

the dominance of the $^3P_1$ and $^3P_0$ products and the nearly equal $^3P_1$: $^3P_0$ ratio indicate that the dissociation mainly occurs on the ^4E state. Due to the extensive overlap of combination bands with the 3_0^8–3_0^{10} transitions, we have been unable to examine how the spin–orbit distributions change between the 3_0^7 and 3_0^{11} transitions.

The interpretation of the vibrational and spin-orbit distributions in terms of which repulsive states contribute to the dissociation are fairly consistent, the main difference being that the the spin–orbit results offers more direct evidence that the $^2A_2$ state plays a role in dissociation following excitation of the 3_0^7 transition. However, the increasing role of the ^4E state at energies above 29 000 cm^{-1} (3.6 eV) is supported by both sets of measurements.

This is consistent with the strength of the spin–orbit coupling between the $\tilde{A}\ ^2A_1$ state and the three repulsive states. Cui and Morokuma[24] have calculated the spin–orbit (SO) coupling matrix elements between the $\tilde{A}\ ^2A_1$ surface and the repulsive $^4A_2$ and ^4E surfaces for CH_3S, finding $H^{SO}(^4A_2,^2A_1)$ and $H^{SO}(^4E,^2A_1)$ to be 75 and 152 cm^{-1}, respectively with minimum seams of crossing located at 3.51 and 3.61 eV above the ground state for the $^4A_2$ and ^4E surfaces, respectively. The SO matrix element $H^{SO}(^2A_2,^2A_1)$ was not calculated for CH_3S. However, based on the analogous calculations for CH_3O, we expect $H^{SO}(^2A_2,^2A_1)$ to be approximately 20% less than $H^{SO}(^4A_2,^2A_1)$. These trends in H^{SO} arise because the dominant electronic configurations for the $\tilde{A}\ ^2A_1$ state and the $^2A_2$ and $^4A_2$ states differ by two spin–orbitals while the ^4E state differs by one spin–orbital.[22,24] In any case, the stronger coupling to the ^4E state state suggests that it should dominate the dissociation once the crossing seam is energetically accessible, and the calculated energy minimum of the crossing seam lies very close to the experimental value at which both the vibrational and spin–orbit distributions change.

B. Excited state lifetimes and mode specificity

Our excited state lifetime measurements as well as previous LIF radiative lifetime measurements[15] show that the predissociation of CH_3S is mode specific, with the ν_3 mode more strongly coupled to the dissociation coordinate than the ν_2 mode. The excited state lifetime decreases from 72 ± 30 ns for the 3_0^3 transition down to 2 ± 2 ps for the 3_0^7 transition over an energy range of approximately 180 meV. The lifetime of the $2_0^1 3_0^n$ transitions is longer than the nearly isoenergetic 3_0^{n+3} transitions and shorter than the 3_0^n transitions indicating that the umbrella mode is not completely decoupled from the dissociation coordinate, but is more weakly coupled than the C–S stretch.

Similar effects have been reported for the $\tilde{A}\ ^2A_1 \leftarrow \tilde{X}\ ^2E$ electronic band of CF_3S based on fluorescence depletion spectroscopy (FDS) linewidth measurements.[55] The $\tilde{A}$ state of CF_3S demonstrates a sharp reduction in lifetime with increased C–S stretch excitation. The lifetime decreases from 38 ns for the first predissociative transition, 3_0^4 located 1211 cm^{-1} above the origin, down to 1.1 ps for the 3_0^8 transition, over an energy range of approximately 150 meV. The lifetimes of the $2_0^1 3_0^n$ combination band transitions of CF_3S display mode-specific behavior analogous to that observed in CH_3S. The $2_0^1 3_0^2$ transition ($0_0^0+1354\ cm^{-1}$) possesses a lifetime of 333 ns, considerably longer than the 3_0^4 transition and shorter than the 2.95 μs lifetime for the 3_0^2 transition ($0_0^0+615\ cm^{-1}$). The lifetimes of these combination band transitions decrease rapidly with increased ν_3 excitation, decreasing down to 0.9 ps for the $2_0^1 3_0^8$ transition ($0_0^0+3082\ cm^{-1}$).

C. Higher excitation energies

Photodissociation of the CH_3S radical following excitation excitation at higher energy is significantly different from that observed for the $\tilde{A}\leftarrow\tilde{X}$ band. The structureless photofragment yield peak, Fig. 7, observed near 45 600 cm^{-1} has a FWHM of $270\pm30\ cm^{-1}$. While this peak is broader than those observed in the predissociative levels of the $\tilde{A}$ state, it is not as broad as one might expect for a completely repulsive surface. The ''narrowness'' of his feature indicates that the electronic state is either bound or relatively flat in the Franck–Condon region. Calculations on the doublet states of CH_3S performed by Hsu *et al.*[14] show that the $\tilde{B}\ ^2A_2$ state is indeed flat in the Franck–Condon region, Fig. 1, due to an avoided crossing between the $\tilde{C}\ ^2A_2$ and $\tilde{B}\ ^2A_2$ states.[22]

The $P(E_T)$ distribution obtained from excitation at 45 600 cm^{-1}, Fig. 8(b), is considerably broader (500 meV) and less structured than the $P(E_T)$ distributions obtained from excitation in the $\tilde{A}\leftarrow\tilde{X}$ band. The fine-structure distribution could not be resolved in the $P(E_T)$ distribution. However, since the dissociation has $\approx$2.6 eV available for translation, we have assumed that the fine-structure distribution from this $^2A_2$ state can be described within the diabatic limit resulting in a statistical fine-structure distribution of 5:3:1.[56] Assuming the excited state to be repulsive, we have attempted to model the product state vibrational distribution using the sudden approximation.

In the sudden limit, the dissociation is sufficiently rapid so that there is minimal coupling between the translational and vibrational degrees of freedom.[1,57] The CH_3 umbrella mode vibrational distribution is obtained by a Franck–Condon projection of the CH_3 group of the excited state methylthio radical onto the CH_3 photofragment. We assume the geometry of the excited state in the Franck–Condon region to be the same as the ground state geometry, i.e., a vertical transition. The ground state $\angle$HCS of 107.8°, derived from $\angle$HCH=111° from the calculations of Janousek *et al.*,[8] is projected onto the planar CH_3 fragment, corresponding to $\angle$HCS=90°. Figure 8(b) shows the results of this calculation convoluted with a statistical fine-structure distribution, an instrument resolution of 40 meV, and a CH_3 Boltzmann rotational distribution with a temperature of 350 K. This model provides a reasonable fit to the experimental data with a vibrational distribution peaking at $\nu_2=2$ and showing excitation up to $\nu_2=5$.

The photofragment anisotropy, $\beta=-0.98$, is consistent with a perpendicular electronic transition indicating that the excited state is either of either $^2A_1$ or $^2A_2$ symmetry. The $P(E_T)$ distribution, Fig. 8(a), shows ground state products, $CH_3+S(^3P)$ to be the dominant dissociation channel

($\geqslant$98%). The $\tilde{B}\ ^2A_2$ state correlates adiabatically to these ground state products. Our results are in contrast to previous photodissociation experiments[22] at 193 nm (51 800 cm^{-1}) in which $S(^1D)+CH_3$ was found to be the primary product channel with $S(^1D):S(^3P)=85:15$. It appears that photodissociation at this energy occurs on a different electronic surface than at 45 600 cm^{-1}. *Ab initio* calculations performed by Hsu *et al.*[14] imply that excitation at 193 nm accesses the bound $\tilde{C}\ ^2A_2$ state which is predissociated by a repulsive ^2E state that correlates to $S(^1D)+CH_3$ products. The combination of our PFY spectrum, the CH_3 vibrational distribution, and the observation of ground state products indicates that dissociation at 45 600 cm^{-1} occurs on the $\tilde{B}\ ^2A_2$ state.

VI. CONCLUSIONS

In this study, we have investigated the photodissociation of CH_3S via the $\tilde{A}\leftarrow\tilde{X}$ and $\tilde{B}\leftarrow\tilde{X}$ bands. For the $\tilde{A}\leftarrow\tilde{X}$ band, we have obtained a structured PFY spectrum containing extended 3_0^n and $2_0^1 3_0^n$ progressions and have determined the onset of predissociation to occur for the 3_0^2 transition.

Measured photofragment anisotropies, $\beta=-0.2$ to -1.0 ± 0.1, have been obtained, consistent with the expected perpendicular transition dipole moment. The measured anisotropies have been used to estimate the excited state lifetimes, which decrease rapidly with increased excitation of the ν_3 mode.

Translational energy $P(E_T)$ distributions have been obtained with sufficient resolution to observe the CH_3 fragment vibrational and $S(^3P_j)$ fine-structure distributions. The fine-structure distributions and vibrational distributions allow us to assess the relative importance of the $^4A_2$, $^2A_2$, and ^4E repulsive electronic surfaces in the predissociation of the $\tilde{A}\ ^2A_1$ state at various photon energies. At photon energies $<$29 000 cm^{-1}, the vibrational and fine-structure distributions suggest that the dissociation takes place on the $^4A_2$ surface, while the increased vibrational excitation and change in fine-structure distributions at higher energies point to dissociation on the ^4E surface. The $2_0^1 3_0^3$ and $2_0^1 3_0^4$ transitions lead to a larger fractional population of the CH_3 fragment umbrella mode than the nearly isoenergetic 3_0^{n+3} transitions, suggesting that the umbrella mode does not couple to the dissociation coordinate as well as the C–S stretch.

Photodissociation of CH_3S at 45 600 cm^{-1} shows $CH_3+S(^3P_{2,1,0})$ to be the dominant product channel, with most of the available energy being partitioned into translation. We have modeled this dissociation using the sudden approximation to describe the vibrational distribution and the diabatic limit to describe the fine-structure distribution. The product channel, photofragment anisotropy, $\beta=-0.98$, and photofragment yield spectra suggest that the excited state is the $\tilde{B}\ ^2A_2$ state.

ACKNOWLEDGMENTS

This research is supported by the Director, Office of Energy Research, Office of Basic Energy Sciences, Chemical Sciences Division, of the U.S. Department of Energy under Contract No. DE-AC03-76F00098. We would like to thank Dr. Qiang Cui for providing ground and excited state geometries, frequencies, and normal coordinates.

[1] R. Schinke, *Photodissociation Dynamics*, 1st ed. (Cambridge University Press, Cambridge, 1993).
[2] L. J. Butler and D. M. Neumark, J. Phys. Chem. **100**, 12801 (1996).
[3] P. L. Houston, J. Phys. Chem. **100**, 12757 (1996).
[4] R. J. Charlson, J. E. Lovelock, M. O. Andreae, and S. G. Warren, Nature (London) **326**, 655 (1987).
[5] A. B. Callear, J. Connor, and D. R. Dickson, Nature (London) **221**, 1238 (1969).
[6] P. C. Engelking, G. B. Ellison, and W. C. Lineberger, J. Chem. Phys. **69**, 1826 (1978).
[7] S. Moran and G. B. Ellison, J. Phys. Chem. **92**, 1794 (1988).
[8] B. K. Janousek and J. I. Brauman, J. Chem. Phys. **72**, 694 (1980).
[9] Y. Endo, S. Saito, and E. Hirota, J. Chem. Phys. **85**, 1770 (1986).
[10] Y. P. Lee, Proc. SPIE **1858**, 44 (1993).
[11] K. Ohbayashi, H. Akimoto, and I. Tanaka, Chem. Phys. Lett. **52**, 47 (1977).
[12] G. Black and L. E. Jusinski, J. Chem. Soc., Faraday Trans. 2 **82**, 2143 (1986).
[13] G. Black and L. E. Jusinski, J. Chem. Phys. **85**, 5379 (1986).
[14] Y.-C. Hsu, X. Liu, and T. A. Miller, J. Chem. Phys. **90**, 6852 (1989).
[15] S.-Y. Chiang and Y. P. Lee, J. Chem. Phys. **95**, 66 (1991).
[16] M. Suzuki, G. Inoue, and H. Akimoto, J. Chem. Phys. **81**, 5405 (1984).
[17] P. Misra, Z. Xinming, and H. L. Bryant, Jr., Pure Appl. Opt. **4**, 587 (1995).
[18] Y.-Y. Lee, S.-Y. Chiang, and Y.-P. Lee, J. Chem. Phys. **93**, 4487 (1990).
[19] A. Kumar, P. K. Chowdhury, K. V. S. Rama Rao, and J. P. Mittal, Chem. Phys. Lett. **198**, 406 (1992).
[20] G. D. Bent, J. Chem. Phys. **92**, 1547 (1990).
[21] R. Fournier and A. E. DePristo, J. Chem. Phys. **96**, 1183 (1992).
[22] C. W. Hsu, C. L. Liao, Z. X. Ma, P. J. H. Tjossem, and C. Y. Ng, J. Chem. Phys. **97**, 6283 (1992).
[23] A. C. Curtiss, R. H. Nobes, J. A. Pople, and L. Radom, J. Chem. Phys. **97**, 6766 (1992).
[24] Q. Cui and K. Morokuma, Chem. Phys. Lett. **263**, 54 (1996).
[25] S. H. S. Wilson, M. N. R. Ashfold, and R. N. Dixon, J. Chem. Phys. **101**, 7538 (1994).
[26] R. E. Continetti, D. R. Cyr, R. B. Metz, and D. M. Neumark, Chem. Phys. Lett. **182**, 406 (1991).
[27] D. J. Leahy, D. L. Osborn, D. R. Cyr, and D. M. Neumark, J. Chem. Phys. **103**, 2495 (1995).
[28] D. L. Osborn, H. Choi, D. H. Mordaunt, R. T. Bise, D. M. Neumark, and C. M. Rohlfing, J. Chem. Phys. **106**, 3049 (1997).
[29] D. L. Osborn, D. J. Leahy, D. R. Cyr, and D. M. Neumark, J. Chem. Phys. **104**, 5026 (1996).
[30] J. M. B. Bakker, J. Phys. E **6**, 785 (1973).
[31] J. M. B. Bakker, J. Phys. E **7**, 364 (1974).
[32] D. P. de Bruijn and J. Los, Rev. Sci. Instrum. **53**, 1020 (1982).
[33] *JANAF Thermochemical Tables*, J. Phys. Chem. Ref. Data **14** (Supplement No. 1) (1985).
[34] R. N. Zare, Mol. Photochem. **4**, 1 (1972).
[35] C. Anastasi, M. Broomfield, O. J. Nielsen, and P. Pagsberg, Chem. Phys. Lett. **182**, 643 (1991).
[36] J. M. Nicovich, K. D. Kreutter, C. A. van Dijk, and P. H. Wine, J. Phys. Chem. **96**, 1992 (1992).
[37] S. Lias, J. E. Bartmess, J. F. Liebman, J. L. Holmes, R. D. Levin, and W. G. Mallard, J. Phys. Chem. Ref. Data **17**, Supplement No. 1 (1988).
[38] S. Nourbakhsh, K. Norwood, H. M. Yin, C. L. Liao, and C. Y. Ng, J. Chem. Phys. **95**, 946 (1991).
[39] S. Nourbakhsh, C.-L. Liao, and C. Y. Ng, J. Chem. Phys. **92**, 6587 (1990).
[40] S. Nourbakhsh, K. Norwood, H. M. Yin, C. L. Liao, and C. Y. Ng, J. Chem. Phys. **95**, 5014 (1991).
[41] B. Russic and J. Berkowitz, J. Chem. Phys. **97**, 1818 (1992).
[42] D. L. Osborn, D. J. Leahy, and D. M. Neumark, J. Phys. Chem. A **101**, 6583 (1997).
[43] H. W. Herman and S. R. Leone, J. Chem. Phys. **76**, 4759 (1982).
[44] C. H. Yamada and E. Kawaguchi, J. Chem. Phys. **75**, 5256 (1981).
[45] J. F. Black, J. R. Waldeck, and R. N. Zare, J. Chem. Phys. **92**, 3519 (1990).
[46] C. Jonah, J. Chem. Phys. **55**, 1915 (1971).

[47] S. Yang and R. Bersohn, J. Chem. Phys. **61**, 4400 (1974).
[48] R. Bersohn and S. H. Lin, Adv. Chem. Phys. **67**, 67 (1969).
[49] M.-C. W. Yang and J. M. Miller, J. Mol. Spectrosc. **186**, 1 (1997).
[50] D. E. Powers, M. B. Pushkarsky, and T. A. Miller, J. Chem. Phys. **106**, 6863 (1997).
[51] X. Lui, C. P. Damo, T. D. Lin, S. C. Foster, and P. Misra, J. Phys. Chem. **93**, 2266 (1989).
[52] D. E. P. Powers, M. B. Yang, and M-C. Miller, J. Phys. Chem. A **101**, 9846 (1997).
[53] D. L. Osborn, D. J. Leahy, E. M. Ross, and D. M. Neumark, Chem. Phys. Lett. **235**, 484 (1995).
[54] H. Lefebvre-Brion and R. W. Field, *Perturbations in the Spectra of Diatomic Molecules* (Academic, Orlando, 1986).
[55] D. E. Powers, M. Pucharsky, and T. A. Miller, Chem. Phys. Lett. **247**, 548 (1995).
[56] S. J. Singer, K. F. Freed, and Y. B. Band, J. Chem. Phys. **79**, 6060 (1983).
[57] R. D. Levine and R. B. Bernstein, *Molecular Reaction Dynamics and Chemical Reactivity* (Oxford University Press, New York, 1987).